

Spectroscopy of Yamato 984028

M.D. Dyar^{a,*}, T.D. Glotch^b, M.D. Lane^c, B. Wopenka^d, J.M. Tucker^a, S.J. Seaman^e,
G.J. Marchand^a, R. Klima^f, T. Hiroi^f, J.L. Bishop^g, C. Pieters^f, J. Sunshine^h

^a Department of Astronomy, Mount Holyoke College, South Hadley, MA 01075, USA

^b Department of Geosciences, Stony Brook University, Stony Brook, NY 11794-2100, USA

^c Planetary Science Institute, 1700 E. Fort Lowell, Suite 106, Tucson, AZ 85719, USA

^d Department of Earth and Planetary Sciences and McDonnell Center for the Space Sciences, Washington University, St. Louis, MO 63130-4899, USA

^e Department of Geosciences, University of Massachusetts, Amherst, MA 01003, USA

^f Department of Geological Sciences, Brown University, Providence, RI 02912, USA

^g SETI Institute/NASA-Ames Research Center, Mountain View, CA 94043, USA

^h Department of Astronomy, University of Maryland, College Park, MD 20742, USA

Received 15 October 2009; revised 16 June 2010; accepted 24 June 2010

Available online 13 July 2010

Abstract

Comprehensive spectroscopic characterization of interior and exterior chips of the Iherzolitic shergottite Y-984028 has been performed using results from six techniques. Data from UV–visible–near-IR reflectance spectra, thermal (mid-IR) emission spectra, attenuated total reflectance (ATR) spectra, transmission FTIR spectra, Raman microprobe spectra, and Mössbauer spectra of whole rock and mineral separates from this meteorite are integrated and compared. Five of these analytical techniques accurately determined the \sim Fo₆₅ composition of the olivine within \pm 10 mol%. Both transmission FTIR and ATR spectra show broad features near 3500 cm⁻¹ indicating the presence of OH/H₂O that does not arise from surface water adsorption. The brown color of the Y-984028 olivine is likely due to the presence of nanophase metallic iron particles (npFe⁰) dispersed throughout the olivine during a major shock event on Mars. Y-984028 olivine also contains a significant amount of Fe³⁺, but this cannot be distinguished from Fe³⁺ that is present in pyroxene and possibly clay minerals. This meteorite and the nakhlite MIL03346 are the two most oxidized of the SNC meteorites studied to date, with Fe³⁺ contents consistent with high-temperature equilibration near the QFM oxygen buffer. © 2010 Elsevier B.V. and NiPR. All rights reserved.

Keywords: Y-984028; Reflectance spectroscopy; Thermal emission spectroscopy; Mössbauer spectroscopy; Raman spectroscopy; Transmission spectroscopy

1. Introduction

Mars exploration is largely dependent on remotely sensed and in situ data for understanding the character and evolution of the surface. Interpretation of the data, in

turn, depends on accurate laboratory data along with solid theoretical understanding. Relations between results from different techniques, however, are often not easily integrated. Each technique has its own theoretical basis and fundamental database using laboratory measurements of materials, but the samples in those databases rarely cross-over from one technique to the

* Corresponding author.

E-mail address: mdyar@mholyoke.edu (M.D. Dyar).

other. Conclusions about compositional properties, for example, are thus very dependent on the specific technique used and may or may not contradict independent measurements with a different technique.

The diversity of sensors available at Mars for mineralogical analyses (e.g., visible to near-infrared, thermal infrared, Mössbauer) enables the uncertainty to be decreased by providing multiple tests for mineral assessment. Unfortunately, very little cross-calibrated laboratory data exist that can be used across multiple sensors for comparison with these results. In this paper, we report carefully planned consortium analyses that produce a full range of spectroscopic data and related detailed information that are the best possible analogs for Mars analyses – namely, data from an actual Mars sample, Y-984028, and minerals therein.

Accordingly, this project seeks to characterize the spectroscopic features of both whole rock and mineral separates from the lherzolitic shergottite Y-984028, in order to place them in the mineralogical context we have established previously through studies of other SNC meteorites. We here integrate results from six different laboratories and report UV–visible–near-mid-IR reflectance spectra, thermal (mid-IR) emission spectra, attenuated total reflectance (ATR) spectra, transmission FTIR spectra, Raman microprobe spectra, and Mössbauer spectra. This work provides spectroscopic insight that will be useful to geochemists studying other aspects of this meteorite and other SNCs. Moreover, we seek to improve our understanding of the spectroscopic features of key minerals and facilitate recognition and interpretation of similar spectroscopic signatures in remotely sensed data from Mars.

2. Methods

We received two samples of the meteorite for study: one from the interior, Y-984028,45 (64 mg), and one from the exterior including fusion crust, Y-984028,74 (87 mg). A carefully sequenced series of measurements were undertaken to facilitate the maximum data return from these valuable samples (Fig. 1). Upon receipt, the two samples were measured at Arizona State University (ASU) to acquire mid-IR thermal emission measurements of the solid rock chips. Following those analyses, one ~20 mg piece was saved from each sample. The remaining whole-rock pieces were then crushed to <125 µm particle size for acquisition of mid-IR thermal emission spectra at Stony Brook University. Following those analyses, the exterior and interior whole-rock samples were each ground and sieved to <45 µm particle size and then analyzed first by UV, visible and near-IR

reflectance spectra at Brown University, then by attenuated total reflectance (ATR) spectra at Stony Brook University, and finally by Mössbauer spectroscopy at Mount Holyoke College.

For analysis of mineral separates, the remaining saved pieces were coarsely crushed (ca. 125 µm grain size) and mid-IR (400–2000 cm⁻¹) emissivity spectra were acquired at Stony Brook University (SBU). Following those analyses, the same samples were handpicked using a binocular microscope into pyroxene and olivine separates, keeping the minerals from the interior and exterior samples separate. It was relatively easy to handpick a pure olivine separate. Pyroxenes, however, tended to be finer-grained and intergrown with olivine, sometimes having possible olivine cores. Given the small amount of sample available for analysis, we picked grains that looked like pyroxene, but we expected that some olivine impurity would show up in various types of spectroscopic analyses of these pyroxene separates. It was not feasible to crush these samples to a small enough particle size to handpick a pure pyroxene separate. It is important to note that both the interior and the exterior chips we received were dominated modally by olivine.

Finally, a few grains of olivine and pyroxene from each piece were reserved for Raman and transmission FTIR measurements, performed at Washington University in St. Louis and the University of Massachusetts in Amherst, respectively.

The mineral separates were analyzed first at the RELAB facility at Brown University (visible to mid-infrared total reflectance studies), where the field of view on each powder sample was about 2.5 mm in diameter; then Stony Brook University (attenuated total reflectance (ATR) spectroscopy and thermal emission spectroscopy); and Mount Holyoke College (Mössbauer spectroscopy). The analyses were done in this order because Mössbauer analysis requires mixing the samples with sugar. All spectroscopic analyses used exactly the same samples, though Raman and transmission FTIR used single crystals extracted from the coarse separate splits before analyses. Raman spectra were acquired on multiple single grains, while transmission FTIR studies were done on doubly polished single crystals ~75 µm thick.

2.1. UV, visible and near to mid-IR spectra

UV, visible and near to mid-IR spectra of the mineral separates and whole-rock particulates were measured in RELAB using the bidirectional reflectance (BDR) spectrometer (0.28–2.6 µm with 5 nm spectral

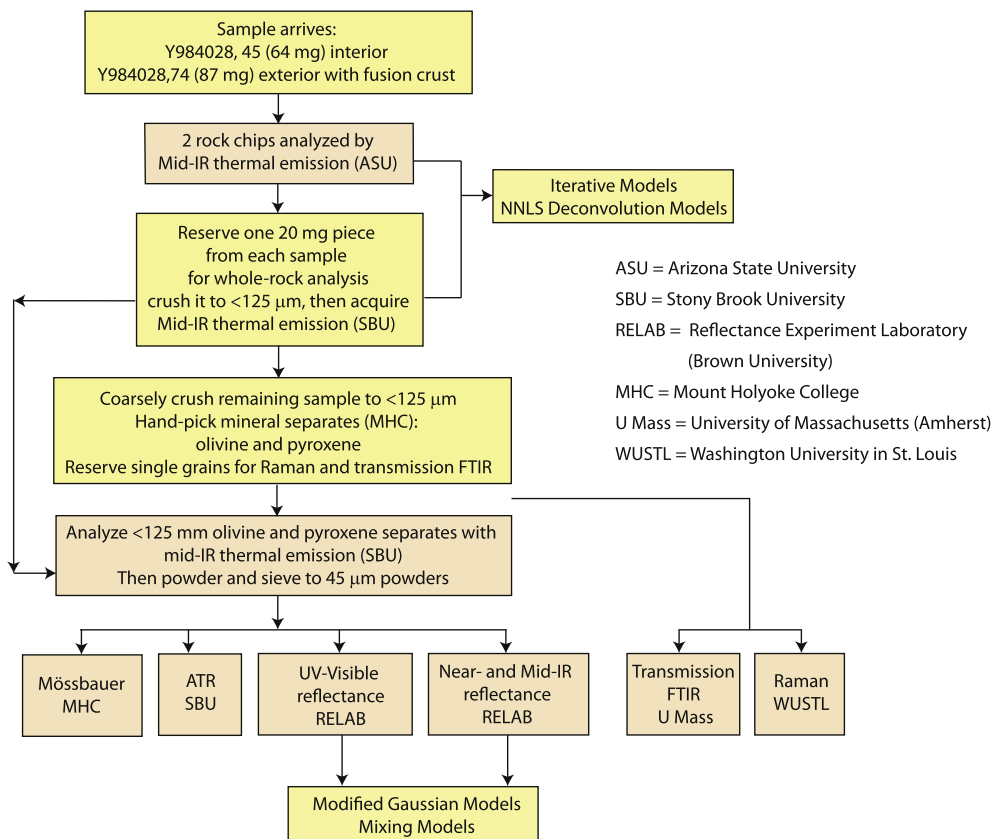


Fig. 1. Schematic showing sample processing and sequence of spectroscopic measurements.

sampling) at 30° incidence and 0° emergence angles. Mid-far IR reflectance spectra were collected using a Thermo-Nicolet Nexus 870 FTIR spectrometer over the wavelength range of $1.8\text{--}50\ \mu\text{m}$ at $4\ \text{cm}^{-1}$ resolution using a diffuse reflectance accessory (biconical, off-axis geometry). These spectra were scaled and spliced to the BDR spectra to provide absolute reflectance.

Absorption bands for visible and near-IR spectra of the interior pyroxene and exterior olivine separates were deconvolved using the Modified Gaussian Model (MGM; Sunshine et al., 1990). The interior olivine spectrum was not modeled, as it exhibits a slight $2\ \mu\text{m}$ band, suggesting contamination from pyroxene. MGM modeling is carried out in apparent absorbance (log reflectance invoking Beer's law). It uses a stochastic inversion to deconvolve a spectrum into a continuum and a series of modified Gaussian curves that can be attributed to specific electronic absorptions (Sunshine et al., 1990; Sunshine and Pieters, 1993). Each absorption band is described by three model parameters: band center, width, and strength. The continuum is a straight-line in energy and is described by two additional parameters, a slope and an offset.

2.2. Thermal (mid-IR) emission spectra

Thermal (mid-IR) emission spectra were acquired at two institutions. The emissivity spectra of the initial meteorite chips were acquired at the ASU Mars Space Flight Facility. The emissivity spectra of the mineral separates (olivine and pyroxene) and the particulate whole rock were acquired at Stony Brook University.

The ASU lab hosts a Nicolet Nexus 670 Fourier transform infrared spectrometer (FTIR). It has been modified for emission measurements by removal of the SiC source and placement of an enclosed glove box and folding mirrors outside the spectrometer housing to enable the energy from a heated sample in a sample chamber to enter into the ray path for measurement. The chamber wall is water-cooled to maintain the environmental temperature. The atmosphere within the spectrometer and sample chamber is scrubbed of CO_2 and H_2O to eliminate their spectral lines from the sample data. The spectrometer is equipped with a thermoelectrically stabilized deuterated triglycine sulfate (DTGS) detector and a CsI beamsplitter that allows quality measurement of emitted radiation over

the mid-infrared range of 2000–240 cm^{-1} (5–42 μm). For each measurement, the meteorite chip was placed in a copper sample cup, painted with Aeroglaze[®] Z302 gloss black paint, and heated to and maintained at an 80 °C set-point for the duration of the measurements. The 240 scans of each sample were acquired at 4- cm^{-1} spectral resolution (2- cm^{-1} spectral sampling) and the individual-scan spectra were averaged together. The resulting sample spectrum was calibrated according to the procedure discussed in detail in Ruff et al. (1997) and converted to spectral emissivity.

Emissivity spectra between 2000 and 370 cm^{-1} were acquired on Stony Brook University's Nicolet 6700 FTIR spectrometer equipped with a KBr beamsplitter and deuterated L-alanine doped triglycine sulfate (DLaTGS) detector. At the time the sample spectra were acquired, the full spectrometer set-up was under construction, so an atmosphere purged of H_2O and CO_2 was not available. Nevertheless, the ambient atmosphere remained constant during the process of measuring both the samples and the calibration targets, so the atmospheric spectral features were corrected for during the spectral calibration. Each particulate sample was placed in an aluminum sample cup painted with Krylon Ultra Flat Black paint. Samples were heated to 80 °C within a water-cooled environmental chamber and maintained at that temperature for the duration of the measurements. A total of 512 scans collected at 2 cm^{-1} sampling was averaged together to produce each final spectrum. Details of the spectral calibration procedure can be found in Ruff et al. (1997).

2.3. Attenuated total reflectance (ATR)

Attenuated total reflectance (ATR) spectra were acquired on Stony Brook University's Nicolet 6700 FTIR spectrometer equipped with a Nicolet SmartOrbit ATR accessory using a type IIa diamond ATR element. The spectrometer was equipped with a thermoelectrically cooled DLaTGS detector with a KBr window and a KBr beamsplitter. The spectrometer was purged with CO_2 - and H_2O -free air. A total of 512 scans acquired at 2 cm^{-1} spectral sampling was averaged to create each final spectrum.

2.4. Transmission FTIR

Transmission FTIR spectra were acquired using a Bruker Vertex 70 FTIR spectrometer equipped with a Hyperion 3000 microscope with both a single element MCT-A detector and a photovoltaic MCT 64 × 64 focal plane array detector in the Department of Geosciences at

the University of Massachusetts. The single element mid-infrared range detector is a DLaTGS detector with a KBr window. The analytical range is extended into the near-infrared with a T304/3 KBr broadband beamsplitter. The microscope is equipped with both 15× and 36× objectives and a ZnSe IR polarizer. The OPUS software package was used for collection and processing of spectra and concentration maps. The beam path is purged with nitrogen gas, and nitrogen gas is exhaled onto the microscope stage to minimize or eliminate atmospheric water and carbon dioxide near the sample. In addition, background spectra are subtracted from sample spectra.

Transmission FTIR spectra are ideal for determining the water contents of nominally anhydrous minerals. Water is typically quantified by relating the height or area of the peak of interest to water concentration. The following form of the Beer–Lambert Law is used for calculating water concentration in glass and nominally anhydrous minerals (Stolper, 1982; Mandeville et al., 2002):

$$c = \left(\frac{18.02 \times \text{absorbance}}{t \times D \times \varepsilon} \right) \quad (1)$$

where c is the weight fraction of water, 18.02 is the molecular weight of water, *absorbance* is the height or area of the absorption peak, t is the thickness in cm, D is the density in g/l, and ε is the absorption coefficient in $\text{L mol}^{-1} \text{cm}^{-1}$ (if peak height is used) or $\text{L mol}^{-1} \text{cm}^{-2}$ (if peak area is used). The 3535 cm^{-1} (2.8 μm) band, which represents the fundamental O–H stretching mode, was used by Stolper (1982) and many subsequent workers (e.g., Dixon et al., 1988; Dixon and Clague, 2001; Saito et al., 2001) to determine total water concentration.

In this study, we used the area of this band, which commonly extends from approximately 2900 to 3700 cm^{-1} , to estimate water concentration in the olivine and pyroxene separates. Absorption coefficients and associated errors are taken from Aubaud et al. (2009): $34\,515 \pm 7050 \text{ L mol}^{-1} \text{cm}^{-2}$ for olivine and $46\,103 \pm 5300 \text{ L mol}^{-1} \text{cm}^{-2}$ for clinopyroxene. Use of the latter coefficient assumes that the pyroxene is from the clinopyroxene sub-group, which cannot be discerned on the basis of the transmission spectra alone but is known from the work of Riches et al. (2010). It should be noted that because their calibrations used samples all with less than 700 ppm H_2O , the results presented here represent extrapolations beyond the bounds of those calibrations and should thus be taken only as estimates. For anisotropic phases such as

olivine and pyroxene, quantitative determination of water concentration requires collection of FTIR spectra from measurement in three mutually orthogonal orientations and summing of concentration measured in each orientation (Libowitzsky and Rossman, 1997; Johnson and Rossman, 2003). The concentrations are related to the sum of the area under the peaks at each of the three orientations using the value of ϵ for a given mineral group. Collection of spectra in three mutually perpendicular orientations from single crystals mounted in epoxy was not possible for this study, so spectra were collected in two random mutually perpendicular orientations, both parallel to the IR beam vibration direction, and their summed water content is multiplied by 3/2.

2.5. Traditional Raman microprobe spectra

Traditional Raman microprobe spectra were recorded at Washington University in St. Louis, using a HoloLab Series 5000 Raman microprobe from Kaiser Optical Systems, Inc. equipped with an axial spectrograph with volume holographic transmission gratings. The excitation wavelength was 532 nm (frequency-doubled Nd-YAG laser). Part of the instrument is a research-grade optical microscope that was used to investigate the sample, focus the laser beam and collect the Raman scattered light. The sample can be viewed at magnifications up to 3200 \times immediately before and after the acquisition of the Raman spectrum in either reflective or transmitted visible light while it is sitting (un-mounted, unprepared) on a glass slide on the microscope's sample stage. This high magnification is achieved through a combination of high-powered objectives (up to 80 \times for this study) and a TV camera/monitor with 40 \times magnification. For this study an 80 \times ultra-long-working-distance objective (Olympus, Japan) with a numerical aperture of 0.75 and a working distance of 8 mm was used for focusing the laser light onto the sample, resulting in a lateral resolution of $\sim 1 \mu\text{m}$ and a power of less than 0.5 mW at the sample surface. With this specific instrument, the whole spectral range of interest in Raman spectroscopy from 100 to 4200 Δcm^{-1} (corresponding to 534–685 nm with 532 nm excitation) can be detected simultaneously with a spectral resolution of 2 cm^{-1} . Raman spectra of most minerals are characterized by very narrow characteristic peaks. The excellent accuracy ($\pm 0.5 \text{ cm}^{-1}$) and precision ($\pm 0.1 \text{ cm}^{-1}$) of peak positions of this instrument over the whole Raman spectral range make it relatively straightforward to identify minerals based on their spectral signatures.

Raman spectra were acquired for four handpicked millimeter-sized grains that were classified (based on their optical properties) as “exterior pyroxene”, “exterior olivine”, “interior pyroxene”, and “interior olivine”. In each of these grains, ~ 10 individual $1 \mu\text{m}$ spots were analyzed. Thus, due to its excellent spatial resolution, Raman analysis does not provide any information of the bulk material, but only of individual spots. Spectra were acquired with the Holograms software (Kaiser Optical Systems, Inc.), and spectral acquisition time per $1 \mu\text{m}$ analysis spot was $32 \times 4 \text{ s}$ (times two because of automated γ -ray filtering). Spectral processing was performed with the Grams/32 Software (Galactic Industries from Thermo Scientific).

2.6. Mössbauer spectroscopy

Approximately 4–12 mg of each sample was crushed under acetone, then mixed with a sugar–acetone solution designed to form sugar coatings around each grain and prevent preferred orientation effects. The amount of sample used was determined by the amount available. Grains were heaped gently in a sample holder confined by Kapton[®] tape. Mössbauer spectra were acquired using a source of $\sim 40 \text{ mCi } ^{57}\text{Co}$ in Rh on a WEB Research Co. Model WT302 spectrometer (Mount Holyoke College) equipped with a scintillation detector. Spectra were acquired at 293 K. Run times were 2–5 days, and baseline counts ranged from 8.8 million to 46 million after the folding and the Compton correction (see Dyar et al., 2009 for details), as needed to obtain reasonable counting statistics for these low-iron, tiny samples. Spectra were collected in 2048 channels and corrected for nonlinearity via interpolation to a linear velocity scale, which is defined by the spectrum of the 25 μm Fe foil used for calibration. To model the data, we used an in-house program generously made available to us by Eddy DeGrave and Toon VanAlboom at the University of Ghent, in Belgium, called Dist3e_DDn (see Dyar et al., 2008 for more information). Quadrupole splittings (Δ), center shifts (δ , referenced to the center of an α -Fe spectrum), and the linewidths (W) of each pair of peaks were allowed to vary. The only additional restriction used was to place a lower limit of 0.24 mm/s on the width of the outermost pyroxene peaks in the interior whole rock and both olivine spectra to prevent unreasonably low linewidths. Ranges of $\pm 0.20 \text{ mm/s}$ on δ and Δ were used to model the very small doublets representing Fe^{3+} . Errors on center shifts and quadrupole splitting are estimated at better than $\pm 0.02 \text{ mm/s}$. Areas were allowed to vary in pairs.

Doublet areas are assumed in this study to directly correspond to the amounts of Fe^{2+} and Fe^{3+} present in the minerals of interest because values for the recoil-free fraction (f) of Fe in each of the sites in all of these minerals are not specifically known (in particular, f_{pyx}^{3+} for any pyroxene composition, and f_{pyx}^{2+} for these pyroxene compositions). Thus the estimated peak errors on results reported here are slightly higher than usual to encompass the possible variation with differential f , as follows. The distribution of area between coexisting Fe^{2+} doublets is non-unique and probably ± 5 – 10% absolute based on comparisons with site occupancies determined by single crystal X-ray diffraction studies. The summed areas of the smaller (e.g., Fe^{3+}) components relative to the total area are estimated to be within ± 3 – 5% absolute based on comparisons with wet chemistry, mineral mixtures, and studies of recoil-free fraction by workers such as Whipple (1968), Dyar et al. (2008), Sklute et al. (2005), and Eeckhout and De Grave (2003).

3. Results and discussion

3.1. Reflectance

Bidirectional visible/near-IR spectra of the particulate samples are shown in Fig. 2. The whole-rock particulate spectrum includes bands centered near 1 and 2 μm that are typical of mixtures of mafic materials dominated by olivine and pyroxene group minerals. The width of the 1 μm band reflects contributions of both pyroxene and olivine absorption bands. Band centers of the pyroxene separates occur near 0.92 and 1.9 μm (Wang et al., 2004) and are consistent with a pyroxene that is low in Ca. Differences were observed for the olivine separates from the interior and exterior of the sample. The 1 μm band in the interior olivine occurs at a slightly shorter wavelength than in the exterior olivine, likely due to slight contamination by pyroxene. This is supported by the presence of a weak 2 μm band in the interior olivine spectrum. Both olivine separates exhibit weaker bands than would be expected for olivine and show a minor “reddening” of the continuum. These properties suggest the presence of minor amounts of nanophase-reduced Fe (or Fe–Ni) in the olivine as observed for NWA 2737 (Pieters et al., 2008). This result is consistent with our own optical microscopy and the report by Mikouchi et al. (2009) that this sample contains brown olivine.

The results of the MGM fit of the exterior olivine are shown in Fig. 3. The band positions for the M2

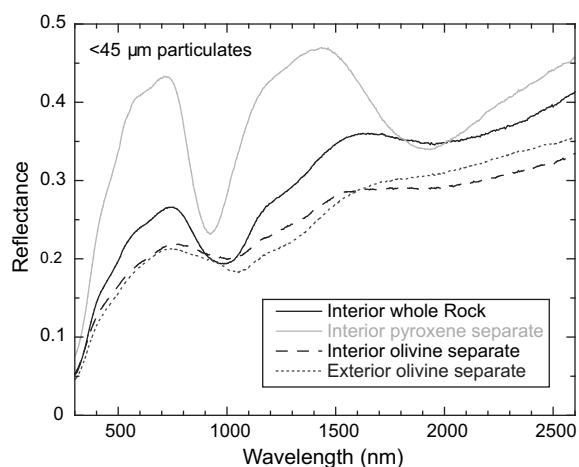


Fig. 2. VNIR reflectance spectra of Y984027 whole-rock interior, as well as pyroxene and olivine separates. Fe^{2+} bands are observed near 1 and 2 μm .

Fe^{2+} band near 1 μm and the M1 Fe^{2+} band near 1.3 μm can be used to estimate the forsterite content of olivine (Sunshine and Pieters, 1998). Though the band centers derived for the Y-984028 olivine are similar to those derived for terrestrial olivine of Fo_{66} from the Kiglipait intrusion (Sunshine and Pieters, 1998; King

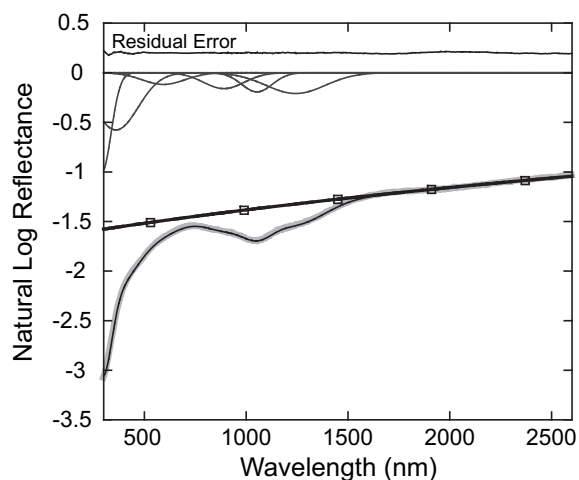


Fig. 3. MGM fit to external olivine mineral separate. Measured reflectance spectrum is shown as a thick grey line, and the model fit is shown as a thin black line. The continuum is shown as a black line with squares, and the deconvolved continuum-removed absorption bands are shown as dark grey lines. All MGM fits were performed using a straight-line continuum in wavelength space. The olivine separate was fit using three bands representing the Fe^{2+} absorptions near 1 μm , and three bands in the visible. All fit parameters were allowed to vary freely. The interior olivine spectrum was not deconvolved, as it exhibits a weak 2 μm band, suggesting contamination from pyroxene or possibly chromite.

and Ridley, 1987), the weakness of the bands and the steep red slope result in a large degree of uncertainty in the model results. Thus, composition based on the band positions would be estimated as roughly $\text{Fo}_{60\pm 10}$, consistent with the Fo_{67} composition measured from olivine close to the fusion crust contact by Riches et al. (2010) but lower than the $\text{Fo}_{91.5}$ reported by them for olivine in the fusion crust itself.

The pyroxene MGM fit was first performed with the assumption that only one type of pyroxene was present in the mineral separate. As illustrated in Fig. 4, the residual error in the single pyroxene fit indicates that an additional band is needed near 2000 nm (2 μm). Because our Raman results (see below) as well as Riches et al. (2010) show evidence of two different pyroxene species in this sample (a clinopyroxene such as augite and a low-Ca orthopyroxene), we experimented with adding a second pyroxene to the model, resulting in a significantly better fit dominated by low-Ca orthopyroxene with some augite also present. It is possible that the second 2 μm band is a slight contamination of the sample with chromite, which also exhibits absorption near 2 μm . This concurs with the report by Riches et al. (2010) that the pyroxenes are intergrown with chromite (present as 3–4% of the mode) within the sample. There is no evidence for the presence of olivine as an “impurity” in this separate that was seen with other techniques (see below). However, these fits cannot conclusively rule out the presence of olivine, which has very weak bands in the 1 μm region.

The exterior pyroxene sample exhibits a spectrum almost identical to the whole-rock particulate and also represents a mixture of mafic minerals. All MGM fits were performed using a straight-line continuum in wavelength space. The olivine separate was fit using three bands representing the Fe^{2+} absorptions near 1 μm and three bands in the visible range. The pyroxene separate was initially fit using three bands in the visible and one band each near 1, 1.2, and 2 μm to represent the M1 and M2 Fe^{2+} absorptions. Additional bands were added as indicated by the residual error from the fit, as shown and described in Fig. 4. All fit parameters were allowed to vary freely.

3.2. Emission

Two emissivity spectra were acquired from the whole-rock exterior meteorite piece (87 mg): (1) a spectrum of the fusion crust alone, which is the outside of the exterior rock chip and (2) a spectrum of the underside of the whole-rock exterior rock chip that

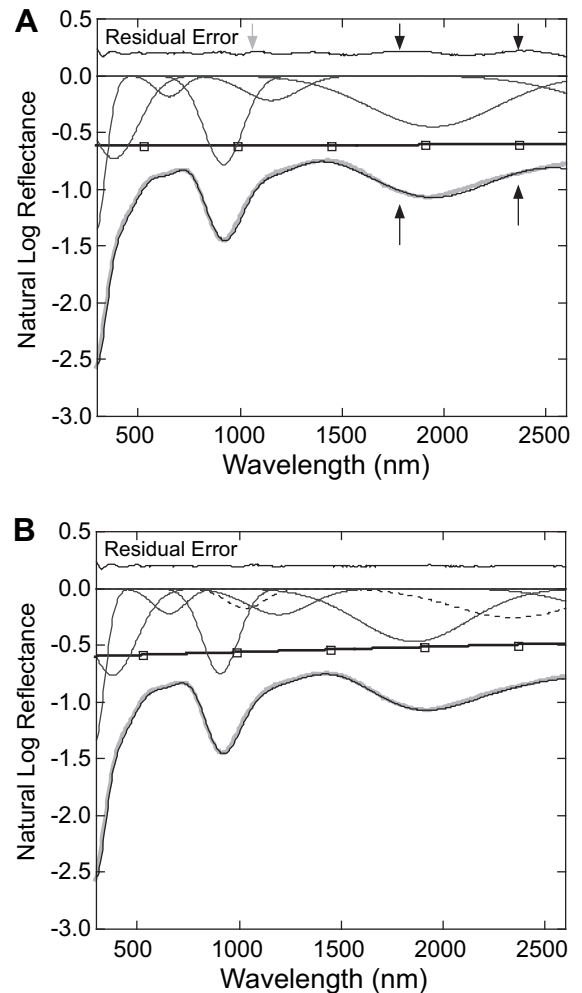


Fig. 4. MGM fits to interior pyroxene mineral separate of Y-984028. (A) *One-mineral fit*: the pyroxene separate was initially fit using three bands in the visible and one band each near 1, 1.2 and 2 μm to represent the M1 and M2 Fe^{2+} absorptions. The residual error from this one-mineral fit suggests that another band is needed in the 2 μm region (black arrows). An additional band may also be necessary near 1 μm (grey arrow). (B) *Two-mineral fit*: additional bands were added, with improvement indicated by the residual error from the fit. The bands attributed to the second phase are shown as dashed lines and is likely to be a higher-Ca pyroxene. The exterior pyroxene sample exhibits a spectrum almost identical to that of the whole-rock particulate and also represents a mixture of mafic minerals.

showed fusion crust in addition to some interior minerals. Two emissivity spectra were also acquired from the whole-rock interior meteorite piece (64 mg), one from each side of the chip (Fig. 5).

The emissivity spectra of the meteorite chips were analyzed using a non-negative least squares (NNLS) linear deconvolution algorithm that simultaneously solves for each component and calculates errors

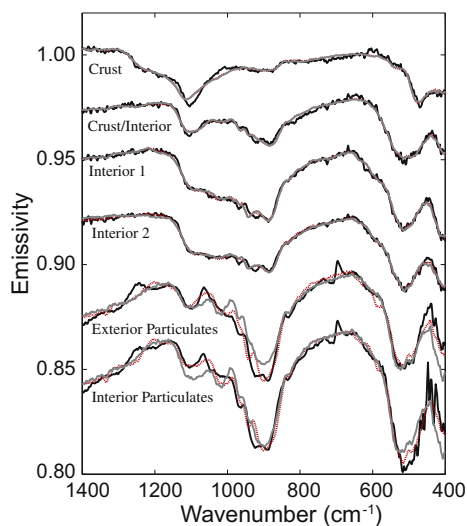


Fig. 5. Emissivity spectra of portions of the chips (crust, crust/interior, Interior 1, and Interior 2) and coarse particulates (exterior particulates and interior particulates) of Y-984028 (black) with the iterative model fits (in grey, Ramsey and Christensen, 1998 model), and the non-negative least square model fits (dotted lines, Rogers and Aharonson, 2008 model). The spectrum labeled “Interior 2” was acquired after the sample piece was turned over.

associated with each mineral group (Rogers and Aharonson, 2008). The model utilized a 53-end-member spectral library to model the composition of the meteorite samples. The library end-members included common rock-forming minerals (feldspars, pyroxenes, olivines, oxides including chromite, micas, other clay minerals, sulfates, and glasses). The black spectra (Fig. 5) are the measured sample spectra while the grey spectra are model fits from the NNLS model. The model results (including RMS values) are shown in Table 1. Note that this method allows different pyroxene species to be identified, so pyroxenes are designated as high-Ca

clinopyroxene (Cpx), low-Ca orthopyroxene (Opx), and pigeonite (which is a specific pyroxene species that happens to be represented in the database).

3.2.1. Exterior/fusion crust chip

The deconvolution model indicates that the fusion crust (i.e., the outside of the exterior rock chip) emissivity spectrum (Fig. 5) is dominated by a silica glass (~50%), as evidenced by its spectral bands at ~1100 (with its higher-frequency shoulder) and 465 cm^{-1} . Additional weaker bands between ~850 and 950 cm^{-1} are due to non-glassy minerals that are also seen clearly in the interior of the meteorite. The model suggests that these additional minerals are olivine, Fe-oxides, and a clinopyroxene sub-group mineral. The underside of the exterior rock chip’s fusion crust (e.g., flip-side crust in Table 1) is dominated by ~45% olivine and a significant amount of pyroxene (~40%, which here includes ~16% pigeonite). Additional components are phyllosilicates (nontronite) at the ~7% level, with ~6% oxide and minor glass. It should be noted that the infrared spectra of glasses and phyllosilicates are similar, hence the models could be using phyllosilicate spectra to model a glassy component in the fusion crust (e.g., Koepfen and Hamilton, 2005). This error is more likely to occur if the fusion crust glass composition is different from the composition of the library glasses. If phyllosilicates are contributing to the spectrum of the fusion crust, they are likely terrestrial weathering products.

3.2.2. Interior chip

The deconvolution model of the “interior” chip emissivity spectrum showed it to be dominated by olivine (~41%) and the clinopyroxene mineral pigeonite (~23%). Other pyroxenes were also identified, as well as plagioclase feldspar. Lesser amounts of

Table 1
Deconvolution results from the NNLS model.

	External crust	Flip-side crust	Interior 1	Interior 2	Exterior coarse ^a	Interior coarse ^a
Plagioclase	0.0 (0)	0.0 (0)	10.0 (0.8)	7.8 (0.8)	16.7 (1.3)	12.0 (1.4)
Clinopyroxene	7.2 (0.8)	20.1 (1.0)	1.2 (0.4)	1.4 (0.5)	8.2 (0.6)	9.4 (0.7)
Orthopyroxene	0.0 (0)	3.3 (1.4)	3.8 (0.8)	8.2 (1.1)	0.0 (0)	1.9 (1.5)
Pigeonite	0.0 (0)	15.8 (2.4)	22.5 (1.2)	25.7 (1.4)	5.9 (1.6)	0.0 (0)
Olivine	33.0 (2.9)	46.5 (1.8)	40.9 (1.3)	38.6 (1.4)	55.1 (2.1)	55.1 (2.0)
Glass	49.9 (0.9)	0.8 (0.6)	12.2 (1.8)	8.5 (1.9)	0.0 (0)	0.0 (0)
Oxides	10.0 (0.9)	5.7 (0.5)	4.8 (0.3)	3.6 (0.3)	13.7 (0.4)	14.0 (0.4)
Phyllosilicates	0.0 (0)	7.4 (1.2)	4.7 (0.7)	6.2 (0.7)	0.0 (0)	3.8 (0.9)
Sulfates	0.0 (0)	0.0 (0)	0.0 (0)	0.0 (0)	0.4 (1.0)	3.8 (0.9)
Total	100.1	100.0	100.1	100.0	100.0	100.0
RMS	0.138	0.121	0.115	0.101	0.299	0.358

^a Coarse samples were coarsely crushed particulates, probably representative of the whole rock.

iron oxides, glass, and phyllosilicates were also identified. After rolling the meteorite pieces to a new position, a second spectrum was acquired (“Interior 2”). The results of this spectral deconvolution are very similar to the initial “Interior 1” sample. This deconvolution model showed the spectrum to be dominated by Mg-bearing olivine (~39%) and pigeonite (~26%), with additional contributions from orthopyroxene, plagioclase, clinopyroxene, iron oxides, and glass/phyllosilicates (Fig. 5).

3.2.3. Whole-rock particulates

We also acquired emissivity spectra of particulates representing the interior and exterior whole-rock compositions (Fig. 5). The deconvolution model (Table 1) indicates that both the interior and the exterior whole-rock particulates are dominated by olivine (~55%) with significant components of iron oxides (~14%) that could be chromite. The model also identifies similar amounts of plagioclase (~12–17%) and pyroxene (~11–14%) in both the interior and the exterior whole-rock particulates.

In general, the model fits to the whole-rock coarse particulates are poor compared to those for the chips, as judged by both the RMS errors (Table 1) and a qualitative assessment of the fit quality (see Fig. 5, comparisons of modeled spectra to the sample spectra). This result is likely due to the fact that the grains were not sieved and consisted of both coarse and fine components, making it more difficult to apply the coarse-particulate library spectra. The effects of fine particulates on the infrared spectra can be seen in the gradual reduction in emissivity at frequencies higher than ~1150 cm⁻¹ (Fig. 5).

There are obvious differences between the model results for the meteorite chips and the particulates derived from the chips (Table 1). For example, the exterior chip spectrum is modeled using ~50% glass, while the particulates derived from that chip are modeled with no glass. This is likely due to the effects of grinding. The glassy fusion crust, while areally significant on the chip is volumetrically small. When the exterior chip was ground into particulates, the fusion crust became areally insignificant compared to the rest of the exterior chip. The result is that glass is not a model component of the exterior particulate spectrum. This effect is also likely responsible for the increased modeled abundance of olivine for the exterior particulate spectrum as compared to the exterior chip. In addition to these surface area effects, it is apparent from Fig. 5 that the particulate samples have some fines mixed in with the coarse particulates. The

presence of fines in the particulate samples results in nonlinear mixing and worse model fits to the spectra as evidenced by the relatively high RMS error values and the poorer fits seen in Fig. 5.

3.2.4. Olivine separates (particulates)

Spectral measurements of the olivine separates (Fig. 6) suggest that the olivine has a composition of ~Fo₆₅ or Fo₇₀ based on the closest match with our library of synthetic olivine spectra, which includes Fo₅₅, Fo₆₅, Fo₇₀, Fo₇₅, as well as many other Fo₀–Fo₁₀₀ increments (Dyar et al., 2009; Lane et al., submitted for publication). As with the Vis/NIR spectra, this composition is a good match to the Fo_{67–74} measured on interior olivines by Riches et al. (2010). The identification of the meteorite olivine composition is based on matching the overall spectral character of the sample spectra to the library emissivity spectra. Fig. 6 shows that the meteorite olivine spectra share specific band positions at 831 and 519 cm⁻¹ (and the emissivity maximum at ~955 cm⁻¹) with the

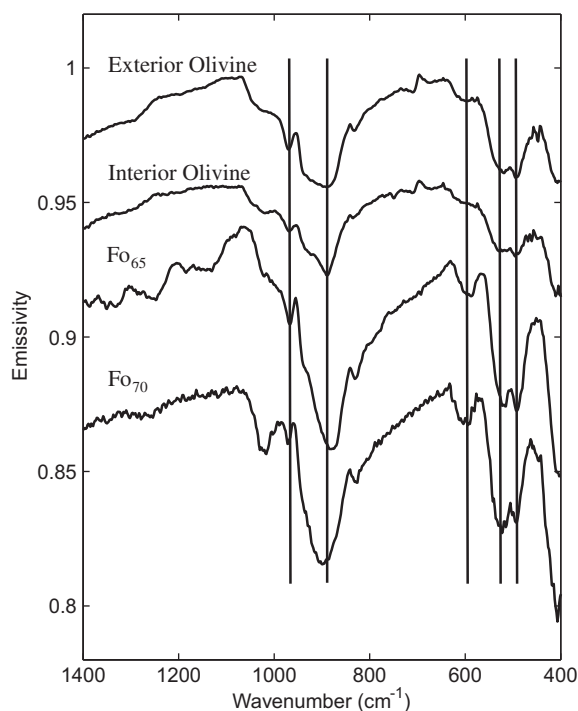


Fig. 6. Emissivity spectra of olivine. The top two meteorite-derived olivine-separate spectra were acquired at SBU and the bottom two synthetic olivine spectra were acquired at ASU. This comparison shows the composition of the Y-984028 olivine to be most similar in composition to Fo₆₅ or Fo₇₀ from Lane et al. (2010). Note: olivine spectra from an entire synthesized Mg- to Fe-olivine suite (Dyar et al. 2009; Lane et al., 2010) were compared to this meteorite. Spectra are offset for clarity.

library Fo₆₅ spectrum and bands 972, 493, and 407 cm⁻¹ with the library Fo₇₀ spectrum. Of these bands, the strong band at 407 cm⁻¹ (for Fo₇₀) is generally optimal for determining olivine composition from a single feature (Lane et al., submitted for publication) because this lattice mode varies in position more than the other bands in Mg–Fe olivine solid solution suite (or is stronger than the ν_4 band that has an equivalent variation in position from forsterite to fayalite) (Lane et al., submitted for publication).

3.2.5. Pyroxene separates (particulates)

The emissivity spectrum of the interior pyroxene separates is consistent with a low-Ca mineral from the clinopyroxene sub-group. The interior pyroxene spectrum has major bands located at 1102, 1000, 964, 928, 881, and 514 cm⁻¹. Deconvolution of the pyroxene separate from the exterior chip shows ~54% total olivine [Fo₆₅ (~45%) and Fo₇₀ (~9%)] with only ~13% of the sample as pyroxene. Additional contributions were suggested from feldspar at ~19% and a fine-grained hematite (~15%, 5–10- μ m-diameter particles). The RMS error of this model fit was 0.292%. An alternate fit to this sample, assuming it to be 100% pyroxene group minerals, looked quite similar to the one, pigeonite spectrum, in our database. Although significant differences exist, the best single-phase match in our database to this spectrum is a synthetic pigeonite with a composition of Wo₁₀En₃₆Fs₅₄ (Fig. 7). Major differences in the spectral features between the synthetic pigeonite and the Yamato Y-984028 pyroxene separates can likely be explained by the Y-984028 sample having a lower Ca content and a higher Mg content than the synthetic pigeonite sample, as reported by Riches et al. (2010).

The pyroxene sample, although handpicked, appears to bear significant amounts of olivine grains that make fitting of the pyroxene sample with a single pyroxene mineral spectrum (or even multiple pyroxene spectra) problematic. Apart from the possible olivine contamination, the possibility exists that the spectral end-member library contains insufficient pyroxene compositions to properly fit the single or multiple phases of pyroxene group minerals that may be present in the meteorite.

Spectra from both the interior and the exterior pyroxene grain separates were also scrutinized for features that might arise from chromite, which is known to be present as inclusions in the Y-984023 pyroxenes (Riches et al., 2010). However, there are no features observed in the emissivity spectra (e.g., a spectral doublet with lobes from ~400 to 560 cm⁻¹

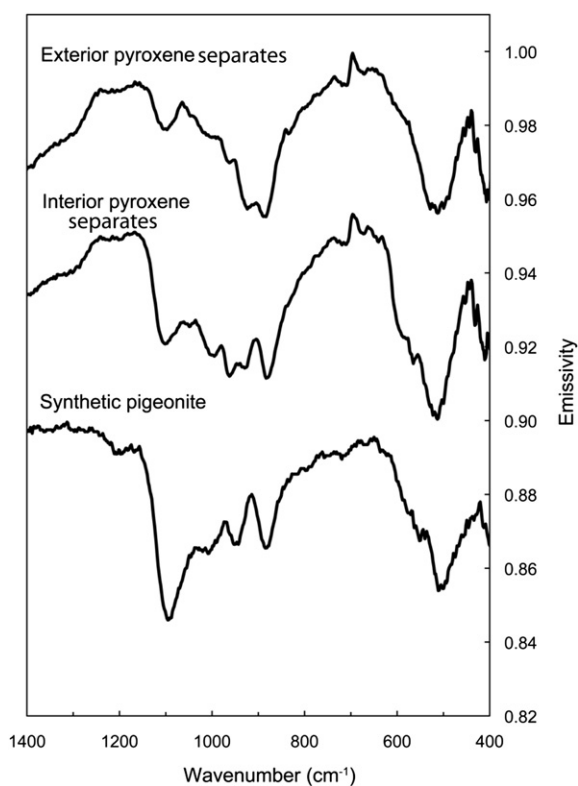


Fig. 7. Emissivity spectra of pyroxene. Spectra of the pyroxene separates were acquired at SBU. The synthetic pigeonite spectrum was acquired at ASU. Spectra are offset for clarity.

and from 560 to 750 cm⁻¹; Lane et al., 2002) that match chromite, as would be seen if the chromite was present as distinct grains. Chromite cores inside the pyroxene grains would not contribute significantly to the measured emissivity spectrum and fine-grained chromite might be difficult to detect, so it is not surprising that chromite is not a modeled component of the pyroxene separate.

3.3. Attenuated total reflectance

Subsequent to the preparation of individual samples as fine powders, there was sufficient material available to acquire ATR spectra of four samples: exterior whole rock, interior whole rock, exterior olivine 45 μ m separate, and interior pyroxene separate (Fig. 8).

Based on the mid-IR data (1400–400 cm⁻¹), the exterior olivine separates are best fit by an olivine composition of ~Fo₇₀. This is evident from absorbance peaks at 969, 863, 833, 602, and 487 cm⁻¹, which are good matches to a synthetic Fo₇₀ ATR spectrum whose correlated peaks occur at 969, 864, 833, 598, and

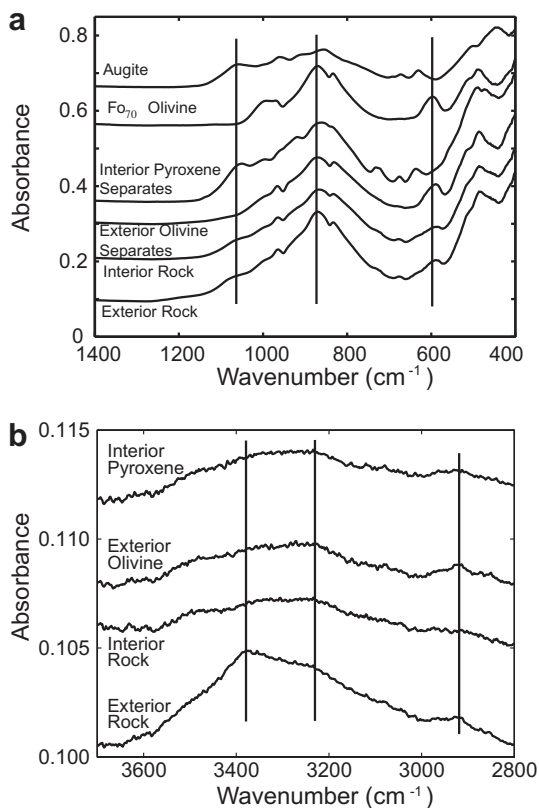


Fig. 8. Attenuated total reflectance (ATR) spectra of four particulate samples of the Y-984028 meteorite. (a) Mid-IR region, where spectral features are due to Si–O and metal–O vibrational modes. (b) Spectral region near the 3 μm water band indicating the presence of a water-bearing phase in the particulate samples. A feature at 2928 cm^{-1} is likely due to the C–H stretching vibrational mode in an organic component.

486 cm^{-1} (Lane et al., submitted for publication). There are no strong peaks in the spectrum of the 45 μm powdered olivine separates that do not correspond to the library Fo_{70} spectrum. This indicates that the contamination of the separates by additional phases is minimal. Mid-IR data of the interior pyroxene separates are not well fit by an existing library pyroxene spectrum. However, the major peaks at 1057, 992, 927, 866, 746, 676, 633, 502, and 458 cm^{-1} are consistent with a mixture of low-Ca and high-Ca clinopyroxenes. Unlike mid-IR emissivity spectra, ATR spectra do not add linearly, so it is difficult to assess the relative contributions of low-Ca and high-Ca clinopyroxenes. Simple inspection of the interior and the exterior rock particulates indicates that they are dominated by olivine with a strong contribution from pyroxene. Additional peaks in the interior and the exterior rock spectra are due to the presence of glass and likely minor feldspar. It is difficult to judge if more minor phases are present.

The ATR data are inconsistent with a significant olivine component being present in the pyroxene separate. Although many of the Si–O vibrational bands in olivine and pyroxene overlap to some degree, olivine has a distinct band at $\sim 600 \text{ cm}^{-1}$ whereas pyroxenes have none. The Yamato pyroxene does not display a band in this region, indicating that any olivine contamination should be at the level of less than a few%. However, note that the emissivity spectra are of coarse particulates while the ATR spectra were taken of fine powders. Riches et al. (2010) note that in at least one zone of their sample, a large pyroxene oikocryst encloses a core olivine grain. In other areas, reactions between olivine and melt cause the growth of pyroxene. It is possible that the grain size difference between what was used for each of these two types of measurements may give rise to biases in what is measured; for example, olivines in pyroxene cores might not show up in the emissivity spectra of coarse particulates.

We also examined shorter wavelength IR data between 2880 and 3600 cm^{-1} . This region contains spectral features of organics and molecularly bound H_2O and OH^- . ATR spectra of each of the four samples show features in this spectral region, although they are broad and roughly an order of magnitude weaker than those in the mid-IR region (Fig. 8). The exterior rock coarse-particulate samples have the strongest features in this region, with absorbance maxima at 3375, 3235, and 2928 cm^{-1} . The first two maxima are part of a broad absorbance peak roughly similar to those seen for hydrated phyllosilicates (Salisbury et al., 1991). The other three spectra all have related peaks in this spectral region, although they are broader and weaker than that seen in the exterior whole-rock spectrum. Based on these spectral features, phyllosilicates may be a minor phase in each of the four samples. The fact that the exterior olivine and especially the exterior rock sample have stronger features than the interior samples suggests that post-impact terrestrial weathering may be primarily responsible for the observed spectral features. Each sample spectrum also has features at ~ 2870 and 2928 cm^{-1} that are consistent with C–H stretching modes and indicate the presence of minor organics (e.g., Bishop et al., 1998; Clark et al., 2009 and references therein). It is not possible to identify whether this feature is indigenous to the samples or the result of post-impact contamination. However, as the C–H bands are much stronger in the spectra of external pieces, the organics are likely due to terrestrial modification.

3.4. Transmission FTIR

FTIR spectra (Fig. 9) acquired on doubly polished single crystals of olivine and pyroxene selected from the exterior and the interior coarse-particulate samples show broad, intense peaks at $\sim 3200\text{--}3600\text{ cm}^{-1}$. These are significantly larger in relative area and are not as sharp as those observed in other SNC single-phase nominally anhydrous crystals or in terrestrial samples. There are several possible explanations for this. As described above, the emission and ATR spectra are consistent with minor phyllosilicates in these samples; even a small amount of phyllosilicate (which can be $\sim 10\text{ wt\% H}_2\text{O}$) could be responsible for the large area of the observed bands. Other workers have reported significant quantities of melt veins and inclusions in this sample (e.g., Riches et al., 2010); it is likely that H_2O , if present in minerals before impact, would migrate into the melt when heated. It is also possible that an effect of shock (feldspar in this sample is nearly entirely maskelynitized; Riches et al., 2010) is to modify the ordered structure of the olivine enough to affect the shape/sharpness of the OH bands.

With these hypotheses as background, the calculated H_2O concentrations can be placed in context (note that despite the reporting convention used here, this H is probably in the form of OH^-). Using olivine and pyroxene absorption coefficients from Aubaud

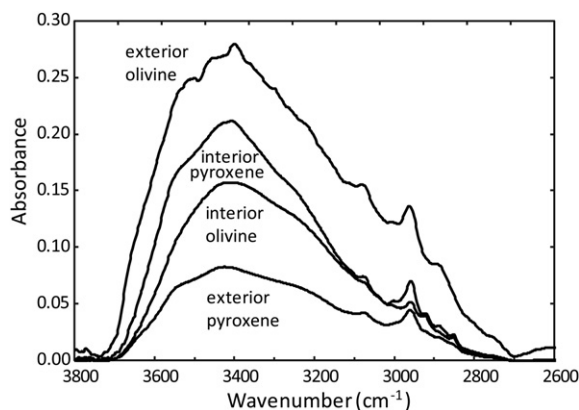


Fig. 9. Baseline-subtracted transmission FTIR spectra of doubly polished $70\text{ }\mu\text{m}$ thick single crystals of olivine and pyroxene extracted from the interior and the exterior chips. To estimate H_2O contents, spectra were acquired with a polarized infrared beam in two mutually perpendicular orientations for each crystal. The Beer–Lambert law was applied to each of the spectra and concentrations calculated from each were summed and multiplied by $3/2$ as an estimate of total water concentration (see explanation in text). As was also seen in the ATR spectra, the samples show minor organic peaks ca. 2930 cm^{-1} .

et al. (2009), $100\text{ }\mu\text{m}$ peak widths, and 3400 g/L for density, calculated H_2O contents are 1800 ppm for external pyroxene and 3500 ppm for interior pyroxene, and 8500 ppm and 3500 ppm for external olivine and interior olivine, respectively. The exterior olivine thus has the largest OH content, consistent with the ATR data and supporting the hypothesis that it represents alteration.

3.5. Raman

Raman spectra obtained on all four types of grains from the coarse particulates were the spectra of silicates (Fig. 10). Raman peak positions do not depend on the orientation of the crystal (with respect to the polarization orientation of the exciting laser beam), whereas the intensities of the Raman active modes for non-cubic crystals can be strongly dependent on orientation. Therefore in randomly oriented samples (such as the minute un-mounted individual grains used here), the intensities of the Raman modes cannot be interpreted, and the scale of the intensity axis is plotted in “arbitrary units”. All peaks of the spectra shown in Fig. 10 can be assigned to Si–O vibrations in silicates with either pyroxene or olivine structure. However, differences can be observed both in the pyroxene

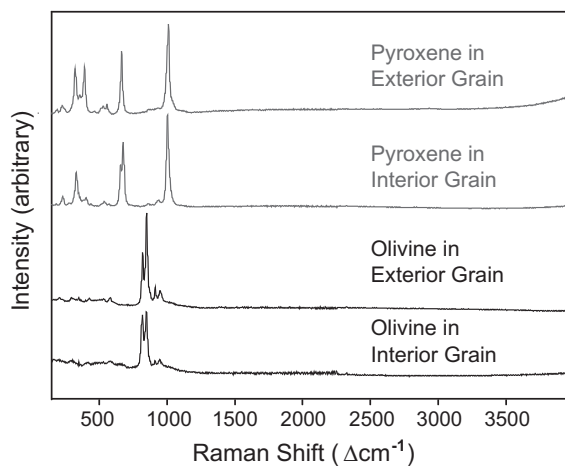


Fig. 10. Typical Raman spectra obtained on optically pre-selected micrometer-sized spots of handpicked external and interior pyroxene and olivine grains, respectively, of the Y-984028 meteorite. Spectra shown are raw, i.e., no background correction, peak smoothing or other spectral manipulations were performed. Blow-ups of detailed spectral regions of the spectra are shown in Figs. 11 and 12. All peaks can be assigned to Si–O vibrations in silicates with either pyroxene or olivine structure. No peaks for O–H stretching vibrations were detected. Thus, the Raman spectra did not show any indication that pyroxenes or olivines in un-mounted handpicked Yamato grains contain either OH^- or H_2O .

structure/composition and the olivine composition in the exterior and interior grains, respectively. No peaks for any O–H stretching vibrations ($>3500 \Delta \text{cm}^{-1}$) were detected in any of the four grains studied. Thus, in contrast to transmission FTIR and ATR results, the Raman spectra did not show any indication that pyroxenes or olivines in un-mounted handpicked Yamato grains contain either OH^- or H_2O .

Raman spectra of the pyroxenes show that exterior and interior grains have distinctive structures corresponding to the clinopyroxene and orthopyroxene subgroups (Fig. 11). Orthopyroxenes always have a doublet near $670 \Delta \text{cm}^{-1}$ that is caused by the symmetric stretching vibration of the Si–O_b–Si bond (O_b is the bridging oxygen) in the $[\text{Si}_2\text{O}_6]_n$ chains. Clinopyroxenes have a single diagnostic peak in this wavenumber region. Because the exact Raman peak positions depend on the force constants of the vibrations (i.e., the strength of the bonds and the angle between bonds) as well as the mass of the participating atoms (i.e., the chemical substitution), they also give (indirect) information about the composition of the pyroxene. In general, the composition of certain minerals can be determined from Raman spectra, as long as there are empirical calibration curves and spectra available that have been acquired on minerals of known chemical composition in solid solutions. Such calibration curves exist for olivines (Kuebler et al., 2006) and pyroxenes (Wang et al., 2001) and rely on

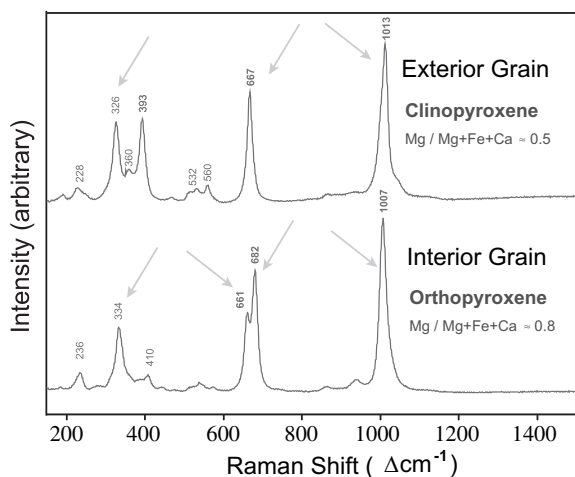


Fig. 11. Raman microprobe spectra show that the pyroxenes in interior and exterior Yamato grains are different. Arrows point to the peaks whose positions are most informative to derive information about the structure and composition of pyroxenes. Estimates of Mg/(Mg + Fe) are based on the positions of two specific peaks (326 and $667 \Delta \text{cm}^{-1}$ in case of top trace) according to the calibration published by Wang et al. (2004).

the exact Raman peak positions. Such calibration data are straightforward for pure solid solution series of MgSiO_4 – FeSiO_4 or MgSiO_3 – FeSiO_3 ; their application and interpretation become more complicated and ambiguous, however, when non- Mg^{2+} and non- Fe^{2+} ionic substitutions occur in the minerals (which, of course, is usually the case in natural minerals). The arrows in Fig. 11 point to the peaks whose positions are most informative for determining both the structure and the composition of pyroxenes. The calibration curve developed by Wang et al. (2001) is based on the exact peak positions of 326 and $667 \Delta \text{cm}^{-1}$ peaks in pyroxenes and makes it possible to estimate Mg-numbers. Based on their calibration curves, the Raman spectra of pyroxenes in Yamato (Fig. 11) are consistent with low-Ca pyroxenes, especially in the case of orthopyroxene found in the interior grains. Thus, the Raman results are in agreement with the results from VNIR spectroscopy and mid-IR emission measurements.

The strongest and most characteristic Raman peaks in olivines are found at ~ 820 and $\sim 850 \Delta \text{cm}^{-1}$, the “olivine doublet” (Fig. 12). The relative wavenumber positions of both peaks in the olivine doublet show monotonic shifts as a function of cation substitution between forsterite and fayalite, and therefore can be used to derive the composition of olivines (Kuebler et al., 2006). Based on comparison to the spectra obtained on our own suite of synthetic standards (Dyar et al., 2009), the composition of the olivine in the exterior grain is most similar to Fo_{80} (Fig. 12). This result agrees with the conclusions from the other types of spectroscopy in this study noted above, as well as with the probe data of Riches et al. (2010).

Seven different micrometer-sized spots in a single external olivine grain were analyzed and three different types of spectra could be grouped in three different types. (1) Very strong olivine spectra with low background were acquired, like the one shown in Fig. 12. (2) One olivine spectrum also showed a peak at $1086 \Delta \text{cm}^{-1}$ that is characteristic for the symmetric C–O stretch in calcite (not shown). The latter spectrum, however, was dominated in intensity by laser-induced fluorescence bands that started at wavenumbers higher than $3631 \Delta \text{cm}^{-1}$ (corresponding to 659 nm). The highest intensity of the laser-induced fluorescence band falls beyond the detection ability of the CCD detector used, and occurred at a wavelength $> 695 \text{ nm}$ and may be associated with the presence of a trace element present in the carbonate lattice. (3) Some spectra showed both the peaks for olivine as well as a broad medium-strength peak centered somewhere between

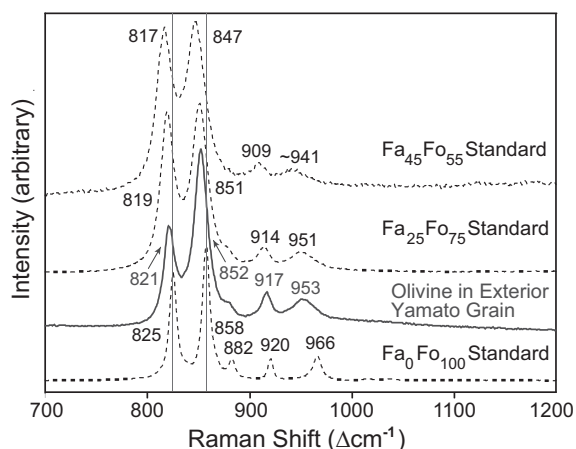


Fig. 12. Raman microprobe spectra of olivines can be used to give chemical information based on the exact peak positions of the Si–O modes within the SiO₄ tetrahedra. As the spectra obtained on synthetic olivine standards (Dyar et al., 2009) show, the Raman peaks shift to lower wavenumbers with greater Fe content in the olivine. Based on such a comparison to the spectra of synthetically produced standards, the olivine in the exterior Yamato grain (whose spectrum is shown here) has a composition close to Fo₈₀.

662 and 685 Δcm^{-1} that could be due to either magnetite, chromite, or ilmenite, which are all weak Raman scatterers and thus rather difficult to detect and identify via Raman spectroscopy.

One of the analyzed interior olivine grains was very inhomogeneous, both optically when investigated in visible reflected light at magnification up to 3200 \times and in terms of its Raman spectra. In addition to clean olivine spectra (example shown in Fig. 10), we also observed in this grain spectra that had: (1) the signature of disordered carbonaceous material (very broad peaks centered at ~ 1374 and $\sim 1590 \Delta \text{cm}^{-1}$); (2) the peaks characteristic of C–H stretching (peaks at 2852, 2899, 2926, and 2963 Δcm^{-1}); and (3) very strong peaks at 215 and 471 Δcm^{-1} that may be caused by elemental sulfur; as well as (4) two very strong peaks at 955 and 971 Δcm^{-1} . The doublet at 955 and 971 Δcm^{-1} is most likely due to P–O symmetric stretching vibrations in a phosphate. Both merrillite and whitlockite always show a split of the P–O stretching mode due to a distortion of the (PO₄)₃-tetrahedra.

Table 2
Mössbauer parameters.

Assignment	Parameter ^a	Whole rock		Olivine		Pyroxene	
		Exterior	Interior	Exterior	Interior	Exterior	Interior
Fe ²⁺ in pyroxene	δ	1.12	1.10			1.13	1.13
	Δ	2.04	2.25			2.17	2.17
	Width	0.34	0.53			0.40	0.31
	Area	0.22	0.31			0.25	0.56
Fe ²⁺ in olivine	δ	1.16	1.17	1.18	1.16		
	Δ	2.99	2.99	2.98	3.01		
	Width	0.23	0.30	0.24	0.32		
	Area	0.19	0.22	0.24	0.39		
Fe ²⁺ in olivine \pm pyroxene	δ	1.11	1.11	1.12	1.12	1.14	1.14
	Δ	2.82	2.78	2.74	2.82	2.83	2.83
	Width	0.31	0.24	0.34	0.32	0.28	0.32
	Area	0.48	0.39	0.34	0.48	0.49	0.32
Fe ³⁺	δ	0.17	0.51	0.29	0.36	0.15	0.11
	Δ	0.55	0.73	0.71	0.61	0.55	0.42
	Width	0.59	0.45	0.60	0.61	0.44	0.66
	Area	0.11	0.09	0.42	0.13	0.14	0.12
Fe ³⁺	δ					0.28	
	Δ					0.96	
	Width					0.34	
	Area					0.12	
	Reduced χ^2	0.6570	1.8920	1.1362	0.9089	0.8905	0.8338
	%Fe ³⁺	11%	9%	42%	13%	26%	12%

^a Values of δ , Δ , and width are given in mm/s; areas are given in % of the total area.

3.6. Mössbauer

Results of fits to the room temperature Mössbauer data are given in Table 2 and shown in Fig. 13. The whole-rock spectra of both the exterior and the interior samples display characteristic (and overlapping) peaks from olivine and pyroxene. Three Fe^{2+} doublets are determined through fitting, with slightly more pyroxene in the interior. All have similar center shifts (~ 1.08 – 1.19 mm/s) but quadrupole splittings vary: 2.04–2.25 mm/s for pyroxene, 2.98–3.01 mm/s for olivine, and 2.74–2.83 mm/s for a doublet that probably contains unresolved contributions from both olivine and pyroxene. The variations in these parameters are likely due to subtle variations in the ratio of orthopyroxene vs. clinopyroxene and to the presence of zoning which introduces compositional variation, which would in turn cause variation in quadrupole splittings.

The bulk rock spectra also contain one poorly resolved Fe^{3+} doublet ($\delta = 0.17$ and 0.51 mm/s; $\Delta = 0.55$ and 0.73 mm/s, respectively) with 9–11% of the total area, but it is not possible to determine which phase(s) are responsible for it. The variation in parameters suggests some possible contribution from Fe-bearing glass, which would have an array of Fe^{3+} sites across the range of 4–6-coordination and cause the δ to vary.

The spectra of olivine separates from both the interior and the exterior samples contain no evidence of pyroxene contamination. The quadrupole splitting of both Fe^{2+} doublets is a match to two-doublet fits of synthetic forsterite spectra (Sklute, 2006) with a composition of Fo_{60-70} , again in agreement with probe data and the other spectroscopic techniques. The interior olivine is 13% Fe^{3+} , but the exterior olivine is significantly more oxidized (42% of the area is in the Fe^{3+} doublet). Such a large amount of Fe^{3+} is unlikely

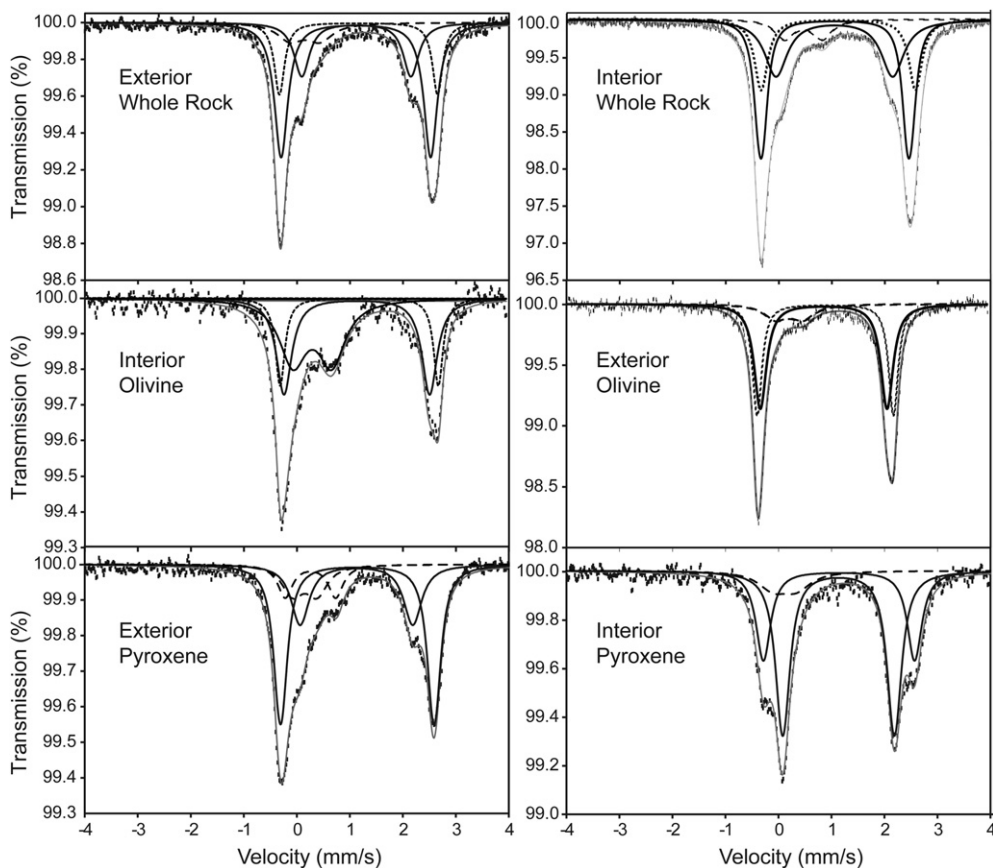


Fig. 13. Mössbauer spectra of crushed whole rock, pyroxene separate, and olivine separate from the exterior (left column) and the interior (right column) of Y-984028 meteorite. Fe^{3+} peaks are shown as long dashed lines, confirmed olivine Fe^{2+} peaks are shown as dotted lines, and pyroxene and undifferentiated pyroxene/olivine Fe^{2+} peaks are shown as black lines. Data points are shown with standard error in the y direction. The fit envelope is a thin grey line running through the data points.

to be present in the olivine structure. Based on the other types of spectroscopic evidence, it is likely to reside in a phyllosilicate such as nontronite (Dyar et al., 2008). Nontronite was the phyllosilicate selected in the mid-IR emissivity deconvolutions for the exterior chip (inner side) and the interior chip (both sides, with other minor phases suggested). This is also consistent with the stronger OH/H₂O features observed in the ATR spectra of the exterior sample, and with the higher OH content of the exterior olivine crystals as measured by transmission FTIR.

The pyroxene spectra from the interior and the exterior chips are also similar to each other. Again, it is the exterior spectrum that is more oxidized (26% vs. 12% in the interior). Both the spectra include one doublet with a position that overlaps with olivine, and in fact, could well be olivine based on comparison with the emissivity spectra of these samples as discussed above. The exterior olivine was modeled with two Fe³⁺ doublets; it is likely that at least one of these could more properly be assigned to a phyllosilicate alteration product as observed by the other techniques.

4. Implications

This multi-wavelength study elucidates many aspects of the chemistry and mineralogy of this sample, as summarized in Table 3. For example, ATR, Raman, and transmission FTIR spectroscopy identified peaks at 2930 cm⁻¹ that represent C–H stretching modes due to minor organics (Clark et al., 2009 and references therein). Of course, many of the results reported by this study can be easily obtained by direct observations using an electron microprobe and transmission electron microscope. However, the advantages of our spectroscopic studies lie in their application to remote sensing of planetary bodies. In this light, it is encouraging to compare the spectroscopic results with those of the petrologic study by Riches et al. (2010) (Table 3).

The various spectral analyses of the pyroxene separate raise two hypotheses about how best to interpret the spectra. For example, the Mössbauer spectra of pyroxenes from the interior and the exterior chips both include a doublet with $\delta = 1.14$ m/s and $\Delta = 2.83$ mm/s that could equally well be assigned to either pyroxene or olivine. The Mössbauer spectra do not differentiate well between orthopyroxenes and clinopyroxenes, so if the doublet is truly pyroxene, then it is unlikely that two different species could be distinguished. On the other hand, Mössbauer spectra of synthetic pyroxene over the Ca–Fe–Mg quadrilateral

show very few 295 K spectra of Fe²⁺ in the M1 site of pyroxene with $\Delta > 2.6$ mm/s, though higher values have been observed in natural samples (Dyar et al., 1989). Contrasted against these results, the ATR data of the same pyroxene separate show no diagnostic olivine band at ~ 600 cm⁻¹, favoring the interpretation that olivine contamination in the pyroxene separate is less than a few %. Finally, the pyroxene sample emissivity deconvolutions can also be modeled either by a combination of pyroxenes or by pyroxene plus olivine; however, the pyroxene-plus-olivine model produces a much better fit to the spectral data than the no-olivine model (i.e., RMS (%) of 0.292 and 0.369 vs. 0.585 and 0.535).

One of the most impressive outcomes of this study is the fact that five of the different analytical techniques used here accurately determined the \sim Fo₆₅ composition of the olivine within ± 10 mol% (Table 3). This compares quite favorably with the electron microprobe results of Riches et al. (2010), who report inter-grain variations in olivine composition ranging from Fo₇₄ to Fo₆₆; Hu et al. (2009) who report Fo_{74.5}–Fe_{66.5}, and Mikouchi et al. (2009) who report Fo_{69–76}. This consistency demonstrates that our ongoing work (Dyar et al., 2009; Lane et al., submitted for publication) on a multi-spectral analysis of synthetic olivines across the Fo–Fa solid solution is making a significant improvement in our capability to determine olivine composition via remote sensing and by Mössbauer spectroscopy.

Our multi-spectral approach provides conflicting evidence for the possible presence of chromite. This phase does not show up in the Mössbauer spectra of any of our samples, even the pyroxene separate; chromite has distinctive doublets that should be resolved even in samples containing olivine and pyroxene, and these are not present. Chromite does not show up in the thermal emission deconvolutions, either, though this could be due to the fact that chromite apparently tends to occur as fine-grained particles in the interiors of pyroxene grains, which might not result in significant characteristic bands in our spectra of coarse particulates. On the other hand, VNIR spectra of fine-grained samples do show a possible chromite signature at ~ 2 μ m, which could also be interpreted to be a second pyroxene band. Finally, Raman spectra show a feature at 662 and 685 Δ cm⁻¹ that could be due either to magnetite, chromite, or ilmenite. In conclusion, the presence or absence of chromite in this meteorite cannot be confirmed, even with the plethora of analytical techniques available. X-ray diffraction analysis of larger aliquots of this sample in the future

Table 3
Integrated summary of techniques used and results.

Technique used	Sample size	Sample type and grain size	Minerals Identified	Other observations
UV–visible reflectance	~10–20 mg	Bulk < 45 μm	Olivine $\text{Fo}_{60\pm 10}$ Low-Ca pyroxene > augite Nanophase Fe or Fe–Ni in olivine	Nanophase Fe probably causes brown color of olivine
Mid-IR thermal emission	~10–20 mg	Bulk < 125 μm	Olivine Fo_{65-70} High-Ca clinopyroxene Low-Ca orthopyroxene Pigeonite: $\text{Wo}_{10}\text{En}_{36}\text{Fs}_{54}$? Phyllosilicates (nontronite?) Oxide (hematite) and minor glass Plagioclase	Spectral end-member library may contain insufficient pyroxene compositions to properly fit these pyroxenes No chromite detected
Attenuated total reflectance	~10–20 mg	Bulk < 45 μm	Olivine Fo_{70} Mix of high-Ca clinopyroxene + low-Ca orthopyroxene Glass Minor feldspar	Weak features observed at $\sim 2880\text{--}3600\text{ cm}^{-1}$ might be hydrated phyllosilicates
Transmission FTIR	~20 \times 30 μm	Single grains doubly polished	Olivine Pyroxene Minor phyllosilicates	Olivine has 3500–8500 ppm H_2O ; pyroxene has 1800–3500 ppm H_2O ; probably represents alteration signature from phyllosilicates
Raman	~20 \times 30 μm	11 single grains	olivine Fo_{80} Fe-rich pyroxene Low-Ca orthopyroxene Oxide	No O–H stretches detected
Mössbauer	~10–20 mg	Bulk < 45 μm	Olivine Fo_{60-70} Pyroxene Fe^{3+} in phyllosilicate	Fe^{3+} highest in exterior, probably due to alteration to Fe^{3+} -rich phyllosilicate; no oxide detected
Riches et al. (2010) thin section petrography and electron microprobe		Thin section	Devitrified fusion crust Olivine Fo_{66-74} Pyroxenes $\sim \text{Wo}_{3-7}\text{En}_{76-71}$ and $\sim \text{Wo}_{23-36}\text{En}_{55-48}$ Chromite, ilmenite, merrillite Pyrrhotite Maskelynite (traces)	Chromite typically enclosed by pyroxene; abundant evidence of shock; melt inclusions common in olivine

might inform this issue and shed light on the possibility of coexisting multiple pyroxenes as well.

The spectroscopic signatures of hydrothermal alteration are evidenced in our spectra through several indicators. Both the transmission FTIR and the ATR data show broad features near 3500 cm^{-1} indicating the presence of OH/H₂O that does not arise from surface water adsorption. The best interpretation of this result would be the presence of some type of phyllosilicate in the exterior portions of the sample. This interpretation is supported by the higher amounts of Fe³⁺ in minerals in the exterior of the meteorite (with Mössbauer parameters corresponding to those of phyllosilicate minerals) and by the fact that the 3 μm band is largest in the exterior minerals (8500 and 1800 ppm in exterior olivine and pyroxene, respectively, vs. 3500 and 3500 ppm in the interiors, respectively). Furthermore, deconvolution models of portions of the meteorite (Table 1) include minor phyllosilicates and ATR data in the 3 μm region are also consistent with their presence. However, it is noteworthy that the existing petrographic studies of this meteorite (Riches et al., 2010; Hu et al., 2009; Mikouchi et al., 2009) do not report significant alteration, suggesting that the phyllosilicate is present at very fine scales such as might only be visible in TEM images.

With regard to the brown color of olivine, this sample may have much in common with another Martian meteorite, the heavily shocked dunite, Northwest Africa (NWA) 2737. The olivines in that meteorite are also very dark and visually brown. Carefully coordinated analyses of NWA 2737 whole rock and olivine separates were reported by Pieters et al. (2008) using visible and near-infrared reflectance, mid-infrared emission and reflectance, and Mössbauer spectroscopic studies of the same samples along with detailed petrography, chemistry, SEM and TEM analyses. The unusual color and spectral properties that extend from the visible through the near-infrared part of the spectrum were shown to be due to nanophase metallic iron particles (npFe⁰) dispersed throughout the olivine during a major shock event on Mars. Given the documented shock history of Y-984028, it is possible that this explanation applies to the brown olivine in it as well. Proof of this hypothesis could come from study of the orientation of different bands of olivine colors as observed in thin section, as was done for NWA 2737 by Treiman et al. (2007), and by careful TEM inspection of the olivine grains to look for nanophase Fe⁰. Mikouchi et al. (2009), who did petrography on a thin section of

this sample, did conclude that the brown color was caused by precipitation of “Fe-rich nanoparticles” in the olivine.

However, the olivine in Y-984028 contains significantly more Fe³⁺ than was observed in NWA 2737: 16–42% of the total iron in the former vs. ~3% in the latter. As noted above, much of this Fe³⁺ is probably present in Fe³⁺-rich clay minerals or glass. It is difficult to determine how much of the Fe³⁺ is in the phyllosilicate and how much is in the olivine because Fe³⁺ peaks have only a small range of velocities and are thus not clearly diagnostic of a particular mineral. If some of the observed Fe³⁺ was associated with the production of nanophase Fe⁰ in olivine, then only a small amount of Fe³⁺ would be produced for the purposes of charge balance (e.g., $3\text{Fe}^{2+} \rightleftharpoons 2\text{Fe}^{3+} + \text{Fe}^0$): ~1–3% of the total iron in olivine would be Fe³⁺ for every ~0.1 vol % npFe⁰, by analogy with NWA 2737 (Pieters et al., 2008) and studies of space weathering (e.g., Noble et al., 2007).

Y-984028 pyroxenes are also oxidized (Table 2), with Fe³⁺ contents of 26% in the exterior chip and 12% in the interior chip. This would be similar to what was observed in pyroxene separates from the MIL03346 augite clinopyroxenite (Dyar et al., 2005), which contained 24% of the total Fe in clinopyroxene as Fe³⁺. The highest known Fe³⁺ contents in all the other SNC meteorites that have been studied is 4.5% in ALHA 84001 (Dyar, 2003). Thus Y-984028 and MIL03346 are the most oxidized of the SNCs by this measure, and Y-984028 is by far the most oxidized of the shergottites. If the Fe³⁺ is only present in a phyllosilicate-like nontronite, then it would suggest that up to one-fourth of the modal mineralogy is phyllosilicate, and this is inconsistent with the petrography (Riches et al., 2010). A better explanation is that this signature is representative of true Fe³⁺ in equilibrium with the pyroxene. This would be consistent with high-temperature equilibration of Y-984028 near the QFM oxygen buffer (McCanta et al., 2004).

In support of this estimate, several studies focusing largely on shergottite meteorites have estimated the oxygen fugacity (f_{O_2}) of Martian basalts. Wadhwa (2001) used Eu/Gd partitioning in augite to show a difference in SNC redox state of more than 3 log units, ranging from QFM-1.6 down to QFM-5. Herd et al. (2001) studied many of the same meteorites using titanomagnetite stoichiometry to calculate oxygen fugacity; he reports a range from QFM-3.0 to QFM-1.0 (± 0.5 log units). A third method for calculating f_{O_2} based on the equilibrium $6\text{FeSiO}_3 + 2\text{Fe}_2\text{O}_3 = 6\text{Fe}_2\text{SiO}_4 + \text{O}_2$ (cf. Wood, 1991) is reported

by Herd et al. (2002) and Herd (2003) that gives a range of f_{O_2} from QFM-3.7 to QFM + 0.2. This range of f_{O_2} would be consistent with the observed Fe^{3+} in Y-984028 pyroxene, and so it appears likely that the Fe^{3+} is indeed in the pyroxene and not all in an alteration phase like a phyllosilicate mineral.

Dyar et al. (2005) hypothesize that this level of oxidation is not uncommon in nakhlites, but our new data require that this hypothesis be expanded to include shergottites as well. Dyar et al. (2005) showed that augites in the NWA817 and Lafayette meteorites also have significant calculated Fe^{3+} . Treiman (2005) reported a calculated Fe^{3+} content of 17% in NWA998. It is unfortunate that aliquots of sufficient size for handpicking of a Mössbauer-quantity clinopyroxene separate are unavailable for these meteorites, which would allow these calculated values to be confirmed by direct observations. But it is apparent that oxidation is persistent in SNC meteorites.

Finally, this study clearly demonstrates the value of using multi-spectral, integrated methods for understanding the complex character and history of samples. A single technique or observation necessarily relies on experience from previous data; in a new setting this may lead to incorrect assumptions. Although this study would have benefited from access to proximal thin sections, our results will certainly support the complementary petrographic and geochemical studies reported in this issue. Together, these studies will further elucidate the chemistry, paragenesis, and history of Y-984028.

Acknowledgments

We thank the curators of the Antarctic Meteorite Research Center, National Institute of Polar Research, Japan for the loan of this sample. Helpful suggestions from two anonymous reviewers and the editor greatly improved this manuscript. We are grateful for support from NASA grant NNX07AR66G from the Mars Fundamental Research Program. Reflectance spectra were acquired using the NASA/Keck RELAB, a multi-user facility supported by NASA grant NNG06GJ31G.

References

Aubaud, C., Bureau, H., Raepsaet, C., Khodja, H., Withers, A.C., Hirschmann, M.M., Bell, D.R., 2009. Calibration of the infrared molar absorption coefficients for H in olivine, clinopyroxene, and rhyolitic glass by elastic recoil detection analysis. *Chem. Geol.* 262, 78–86.

Bishop, J.L., Pieters, C.M., Hiroi, T., Mustard, J.F., 1998. Spectroscopic analysis of Martian meteorite ALH 84001 powder and applications for spectral identification of minerals and other soil components on Mars. *Meteorit. Planet. Sci.* 33, 699–708.

Clark, R.N., Curchin, J.M., Hoefen, T.M., Swayze, G.A., 2009. Reflectance spectroscopy of organic compounds: 1. Alkanes. *J. Geophys. Res.* 114, E03001. doi:10.1029/2008JE003150.

Dixon, J.E., Clague, D.A., 2001. Volatiles in basaltic glasses from Loihi seamount, Hawaii: evidence for a relatively dry plume component. *J. Petrol.* 42, 627–654.

Dixon, J.E., Stolper, E., Delaney, J., 1988. Infrared spectroscopic measurements of CO_2 and H_2O in Juan de Fuca Ridge basaltic glasses. *Earth Planet. Sci. Lett.* 90, 87–104.

Dyar, M.D., 2003. Ferric iron in SNC meteorites as determined by Mössbauer spectroscopy: implications for Martian landers and Martian oxygen fugacity. *Meteorit. Planet. Sci.* 38, 1733–1752.

Dyar, M.D., McGuire, A.V., Ziegler, R.D., 1989. Redox equilibria and crystal chemistry of coexisting minerals from spinel lherzolite mantle xenoliths. *Am. Mineral.* 74, 969–980.

Dyar, M.D., Schaefer, M.W., Sklute, E.C., Bishop, J.L., 2008. Mössbauer spectroscopy of phyllosilicates: effects of fitting models on recoil-free fractions and redox ratios. *Clay Miner.* 43, 3–33.

Dyar, M.D., Sklute, E.C., Menzies, O.N., Bland, P.A., Lindsley, D., Glotch, T., Lane, M.D., Wopenka, B., Klima, R., Bishop, J.L., Hiroi, T., Pieters, C.M., Sunshine, J., 2009. Spectroscopic characteristics of synthetic olivines: an integrated multi-wavelength and multi-technique approach. *Am. Mineral.* 94, 883–898.

Dyar, M.D., Treiman, A.H., Pieters, C.M., Hiroi, T., Lane, M.D., O'Connor, V., 2005. MIL03346, the most oxidized Martian meteorite: a first look at spectroscopy, petrography, and mineral chemistry. *J. Geophys. Res.* 110, E09005. doi:10.1029/2005JE002426.

Eeckhout, S.G., De Grave, E., 2003. Evaluation of ferrous and ferric Mössbauer fractions. Part II. *Phys. Chem. Miner.* 30, 142–146.

Herd, C.D.K., Papike, J.J., Brearley, A.J., 2001. Oxygen fugacity of Martian basalts from electron microprobe oxygen and TEM–EELS analyses of Fe–Ti oxides. *Am. Mineral.* 86, 1015–1024.

Herd, C.D.K., Schwandt, C.S., Jones, J.H., Papike, J.J., 2002. An experimental and petrography investigation of Elephant Moraine 79001 lithology A: implications for its petrogenesis and the partitioning of chromium and vanadium in a Martian basalt. *Meteorit. Planet. Sci.* 37, 987–1000.

Herd, C.D.K., 2003. The oxygen fugacity of olivine-phyric Martian basalts and the components within the mantle and crust of Mars. *Meteorit. Planet. Sci.* 38, 1793–1805.

Hu, S., Feng, L., Lin, Y.T., 2009. Petrography and mineral chemistry of the Y984028 lherzolitic shergottite. *Antarct. Meteor.* XXXII, 22–23.

Johnson, E.A., Rossman, G.R., 2003. The concentration and speciation of hydrogen in feldspars using FTIR and 1H MAS NMR spectroscopy. *Amer. Mineral.* 88, 901–911.

King, T.V.V., Ridley, W.I., 1987. Relation of the spectroscopic reflectance of olivine to mineral chemistry and some remote sensing implications. *J. Geophys. Res.* 92, 11,457–11,469.

Koepfen, W.C., Hamilton, V.E., 2005. Discrimination of glass and phyllosilicate minerals in thermal infrared data. *J. Geophys. Res.* 110 (E08006). doi:10.1029/2005JE002474.

Kuebler, K.E., Jolliff, B.L., Wang, A., Haskin, L.A., 2006. Extracting olivine (Fo–Fa) compositions from Raman spectral peak positions. *Geochim. Cosmochim. Acta* 70, 6201–6222.

- Lane, M.D., Morris, R.V., Mertzman, S.A., Christensen, P.R., 2002. Evidence for platy hematite grains in Sinus Meridiani, Mars. *J. Geophys. Res.* 107 (E12), 5126. doi:10.1029/2001JE001832.
- Lane, M.D., Glotch, T.D., Dyar, M.D., Pieters, C.M., Klima, R., Hiroi, T., Bishop, J.L., Sunshine, J. Midinfrared spectroscopy of synthetic olivines: thermal emission, attenuated total reflectance, and specular and diffuse reflectance studies of forsterite to fayalite. *J. Geophys. Res.*, submitted for publication.
- Libowitzky, E., Rossman, G.R., 1997. An IR absorption calibration for water in minerals. *Am. Mineral.* 82, 1111–1115.
- Mandeville, C.W., Webster, J.D., Rutherford, M.J., Taylor, B.E., Timbal, A., Faure, K., 2002. Determination of molar absorptivities for infrared absorption bands of H₂O in andesitic glasses. *Am. Mineral.* 87, 813–821.
- McCanta, M.C., Dyar, M.D., Rutherford, M.J., Delaney, J.S., 2004. Iron partitioning between basaltic melts and clinopyroxene as a function of oxygen fugacity. *Am. Mineral.* 89, 1685–1693.
- Mikouchi, T., Satake, W., Kurihara, T., 2009. Y-984028 lherzolithic shergottite: a new Antarctic find likely paired with Y000027/000047/000097. *Antarct. Meteor. XXII*, 35–36.
- Noble, S.K., Pieters, C.M., Keller, L.P., 2007. An experimental approach to understanding the optical effects of space weathering. *if the 192*, 629–642.
- Pieters, C.M., Klima, R., Hiroi, T., Dyar, M.D., Lane, M.D., Treiman, A.H., Noble, S., Sunshine, J., Bishop, J., 2008. The origin of brown olivine in Martian dunite NWA 2737: integrated spectroscopic analyses of brown olivine. *J. Geophys. Res.* doi:10.1029/2007JE002939.
- Ramsey, M.S., Christensen, P.R., 1998. Mineral abundance determination: quantitative deconvolution of thermal emission spectra. *J. Geophys. Res.* 103, 577–596.
- Riches, A.J.V., Liu, Y., Day, J.M.D., Puchtel, I.S., Rumble III, D., McSween Jr., H.Y., Walker, R.J., Taylor, L.A., 2010. Petrology and geochemistry of Yamato 984028: cumulate lherzolithic shergottite with affinities to Y 000027, Y 000047, and Y 000097. *Polar Sci.* 4 (4), 497–514.
- Rogers, A.D., Aharonson, A., 2008. Mineralogical composition of sands in Meridiani Planum determined from Mars Exploration Rover data and comparison to orbital measurements. *J. Geophys. Res.* 113, E06S14. doi:10.1029/2007JE002995.
- Ruff, S.W., Christensen, P.R., Barbera, P.W., Anderson, D.L., 1997. Quantitative thermal emission spectroscopy of minerals: a laboratory technique for measurement and calibration. *J. Geophys. Res.* 102, 14899–14913.
- Saito, G., Kazahaya, K., Shinohara, H., Stimac, J., Kawanabe, Y., 2001. Variation of volatile concentration in a magma system of Satsuma-Iwojima volcano deduced from melt inclusion analyses. *J. Volc. Geotherm. Res.* 108, 11–31.
- Salisbury, J.W., Walter, L.S., Vergo, N., D'Aria, D.M., 1991. *Infrared (2.1–25 μm) Spectra of Minerals*. Johns Hopkins University Press, Baltimore.
- Sklute, E.C., 2006. Mössbauer spectroscopy of synthetic olivine across the Fe–Mg solid solution. B.A. thesis. Mount Holyoke College, South Hadley, MA.
- Sklute, E.C., Rothstein, Y., Schaefer, M.W., Menzies, O.N., Bland, P.A., Berry, F.J., 2005. Temperature dependence and recoil-free fraction effects in olivines across the Mg–Fe solid solution. *Lunar Planet. Sci. XXXVI*, Abstract #1888.
- Stolper, E., 1982. Water in silicate glasses: an infrared spectroscopic study. *Contrib. Mineral. Petrol.* 81, 1–17.
- Sunshine, J.M., Pieters, C.M., Pratt, S.F., 1990. Deconvolution of mineral absorption bands: an improved approach. *J. Geophys. Res.* 95, 6955–6966.
- Sunshine, J.M., Pieters, C.M., 1993. Estimating modal abundances from the spectra of natural and laboratory pyroxene mixtures using the modified Gaussian model. *J. Geophys. Res.* 98, 9,075–9,087.
- Sunshine, J.M., Pieters, C.M., 1998. Determining the composition of olivine from reflectance spectroscopy. *J. Geophys. Res.* 103, 13,675–13,688.
- Treiman, A.H., Dyar, M.D., McCanta, M., Pieters, C.M., Hiroi, T., Lane, M.D., Bishop, J., 2007. Martian dunite NWA 2737: petrographic constraints on geologic history, shock events, and olivine color. *J. Geophys. Res.* 112, E04002. doi:10.1029/2006JE002777.
- Treiman, A.H., 2005. The nakhlite Martian meteorites: Augite-rich igneous rock from Mars. *Chem. Erde* 65, 203–270.
- Wadhwa, M., 2001. Redox state of Mars' upper mantle and crust from Eu anomalies in shergottite pyroxenes. *Science* 291, 1527–1530.
- Wang, A., Jolliff, B.L., Haskin, L.A., Kuebler, K.E., Viskupic, K.M., 2001. Characterization and comparison of structural and compositional features of planetary quadrilateral pyroxenes by Raman spectroscopy. *Am. Mineral.* 86, 790–806.
- Wang, A., Kuebler, K., Jolliff, B., Haskin, L.A., 2004. Mineralogy of a Martian meteorite as determined by Raman spectroscopy. *J. Raman Spectrosc.* 35, 504–514.
- Whipple, E.R., 1968. Quantitative Mössbauer spectra and chemistry of iron. In: *Earth and Atmospheric Science*, vol. 187. Massachusetts Institute of Technology, Cambridge.
- Wood, B.J., 1991. Oxygen barometry of spinel peridotites. *Revs. Mineral.* 14, 417–431.